Journal of
Materials Chemistry A

Materials for energy and sustainability

Accepted Manuscript

This article can be cited before page numbers have been issued, to do this please use: W. Tian, R. Sato, T. Uchiyama, Y. Tatetsu, K. Matsumoto, Y. Uchimoto and T. Teranishi, *J. Mater. Chem. A*, 2026, DOI: 10.1039/D5TA08256K.

This is an Accepted Manuscript, which has been through the Royal Society of Chemistry peer review process and has been accepted for publication.

Accepted Manuscripts are published online shortly after acceptance, before technical editing, formatting and proof reading. Using this free service, authors can make their results available to the community, in citable form, before we publish the edited article. We will replace this Accepted Manuscript with the edited and formatted Advance Article as soon as it is available.

You can find more information about Accepted Manuscripts in the Information for Authors.

Please note that technical editing may introduce minor changes to the text and/or graphics, which may alter content. The journal's standard Terms & Conditions and the Ethical guidelines still apply. In no event shall the Royal Society of Chemistry be held responsible for any errors or omissions in this Accepted Manuscript or any consequences arising from the use of any information it contains.

ROYAL SOCIETY OF CHEMISTRY

rsc.li/materials-a

View Article Online
DOI: 10.1039/D5TA08256K

ARTICLE

Zinc-Induced Ordering in $L1_0$-Type Platinum-Based Nanoalloys for the Electrocatalytic Oxygen Reduction Reaction

Received 00th January 20xx,
Accepted 00th January 20xx

DOI: 10.1039/x0xx00000x

Wu Tian,[a] Ryota Sato,[*b] Tomoki Uchiyama,[†c] Yasutomi Tatetsu,[d] Kenshi Matsumoto,[b] Yoshiharu Uchimoto,[c] and Toshiharu Teranishi[*ab]

Platinum (Pt)-based intermetallic compound (IMC) nanoparticles (NPs) show high activity and durability in the oxygen reduction reaction (ORR) even in the highly acidic environment of polymer electrolyte fuel cells. Although Pt-based IMCs with $L1_0$ crystal structure have been thoroughly studied, further improvement of ordering degree is required to enhance their ORR catalytic performance. Typical syntheses of $L1_0$-ordered Pt*M* (*M* is usually a 3*d* transition metal) IMC NPs require high-temperature annealing to induce the disorder–order transformation, which leads to unfavorable NP aggregation. Given that $L1_0$-PtZn has a much lower phase transformation temperature than other $L1_0$-Pt*M*, Zn was included to allow the phase transformation of $L1_0$-Pt(*M*,Zn) NPs to occur at relatively low temperature, thus suppressing aggregation and increasing the average ordering degree of NPs. We fabricated sub-6-nm $L1_0$-Pt(*M*,Zn) NPs with a high ordering degree (>80%) through a facile wet chemical route followed by low-temperature annealing. Lattice constant tuning achieved by precise composition control revealed a positive correlation between the strain effect and corresponding ORR activity. Highly ordered $L1_0$-$Pt_5Co_4Zn_1$ and $L1_0$-$Pt_5Ni_4Zn_1$ NPs showed high specific activities of 1.71 and 1.40 mA/cm$^2_{Pt}$, respectively, which are almost comparable to that of $L1_0$-PtCo NPs.

1. Introduction

A proton-exchange membrane fuel cell (PEMFC) can be defined as a galvanic cell that converts chemical energy directly into electrical energy. PEMFC s show promise as a type of next-generation energy source because of their advantages including fast fueling, high energy density, and zero pollution.[1] However, the high cost, low efficiency, and short life time of the catalysts for the cathodic oxygen reduction reaction (ORR) are major technical obstacles for the production of commercially feasible PEMFC s. After decades of research developing highly efficient ORR catalysts, scarce and expensive platinum (Pt) is still an indispensable core component of cathodic ORR catalysts.

Recent studies have shown that incorporation of transition metals (*M*) with smaller atomic radius (such as Fe, Co, Ni, Cu, etc.) into Pt nanoparticles (NPs) introduces beneficial compressive strain into the Pt-rich atomic layers that are formed on the outermost surface by acid treatment. A theoretical study suggested that compressive surface strain in the Pt layer weakens its binding with oxygen intermediates, thus increasing the cathodic ORR performance of Pt*M*-Pt core–shell (Pt*M*@Pt) catalysts.[2] As highlighted by Pt_3Ni@Pt nanoframes,[3] PtNi@Pt bunched nanocages,[4] and Pt_3Co@Pt NPs,[5] both alloying Pt with *M*, especially Co and Ni with quite small atomic radii, and constructing core–shell structures with Pt-rich surfaces can induce a compressive strain effect in the Pt outermost layer, which can effectively accelerate ORR kinetics as well as lower the Pt content of the catalysts. Although some catalysts achieved high ORR performance, most current Pt-based catalysts suffer from poor durability because of the leaching of *M* in the strongly acidic electrolyte at high potential, which leads to structural changes that decrease activity.

To prevent *M* leaching from Pt*M* NPs, highly ordered Pt*M* intermetallic compounds (IMCs) with well-defined stoichiometry have attracted much attention as stable core materials for surface strain-engineered Pt*M*@Pt NPs recently. Pt*M* IMCs possess higher acid corrosion resistance than that of disordered Pt*M* NPs because of their larger formation enthalpy.[6, 7] There are already multiple reports on the synthesis of binary $L1_0$-Pt*M* and ternary $L1_0$-type Pt (M_1,M_2) NPs as high-performance ORR catalysts including $L1_0$-PtZn,[8] $L1_0$-PtNi,[9, 10] $L1_0$-PtCo,[6, 11-13] $L1_0$-PtFe,[7] and $L1_0$-PtCoNi.[14, 15] Low-temperature synthesis of Pt-based IMC NPs containing *M* with high melting points (Fe: 1535 °C; Co: 1495 °C; Ni: 1453 °C) is challenging even though Pt IMCs are thermodynamically more favourable than their solid-solution counterparts at room temperature.[16] High-temperature thermal annealing is usually required to induce phase transformation from disordered Pt*M* alloys into ordered Pt*M* IMCs in the solid state by overcoming the high energy barrier for atom diffusion to achieve ordering.[17, 18] High-

[a] Department of Chemistry, Kyoto University, Uji, Kyoto 611-0011, Japan.
[b] Institute for Chemical Research, Kyoto University, Uji, Kyoto 611-0011, Japan.
[c] Graduate School of Human and Environmental Studies, Kyoto University, Sakyo-ku, Kyoto 606-8501, Japan.
[d] Department of Health Informatics, Meio University, Biimata, Nago, Okinawa 905-8585, Japan
† Present Addresses: Department of Metallurgy, Materials Science and Materials Processing, Tohoku University, Sendai, Miyagi 980-8579, Japan.

temperature annealing causes severe sintering of NPs, especially when at high NP loading on supports, resulting in a large decrease of the specific surface area (surface-to-volume ratio) of the NPs. In addition, the long-range order parameter (*S*) that quantifies the ordering degree is compromised when the annealing temperature exceeds the relatively lower phase-transition temperature (T_{PT}) from an $L1_0$-type IMC to *A*1-type solid solution in the corresponding bulk Pt–*M* binary phase diagram (T_{PT}: PtFe ~1300 °C, PtCo ~820 °C, PtNi ~630 °C).[9] For NPs with high specific surface area, T_{PT} decreases because of the increased contribution of entropy as a function of temperature in the Gibbs free energy equation resulting from the increased exposure of the disordered surface. Thus, as a problem unique to NPs with a size distribution, a situation may arise where smaller particles with *A*1 structure and particles with $L1_0$ structure that are larger than a critical particle size coexist depending on the heat treatment temperature. As a result, the average *S* for ensemble NPs tends to decrease with particle size. The *S* achieved after thermal annealing, which is the key parameter to improve the electrocatalytic performance of $L1_0$-Pt*M*, has seldom been discussed in previous studies. A feasible way to improve the ordering degree of small IMC NPs and thus increase the activity and durability of ORR catalysts for fuel-cell applications still needs to be demonstrated.

The introduction of low-melting-point metals into IMC nanoparticles (NPs) is a promising strategy for lowering the activation energy of atomic diffusion.[17-21] Elements from groups 12–15 are suitable candidates due to their low melting points, such as Zn (420 °C), Cd (321 °C), Ga (30 °C), In (157 °C), Sn (232 °C), Pb (328 °C), and Bi (~271 °C). However, incorporating such metals may reduce the compressive strain in the surface Pt atomic layers, thereby decreasing the specific activity for the oxygen reduction reaction (ORR), because most of these metals have larger atomic radii than 3d transition metals such as Co and Ni (atomic radius: Co ~125 pm, Ni ~125 pm). Among these low-melting-point metals, we selected Zn because it has a relatively small atomic radius (134 pm) and forms a thermodynamically stable $L1_0$ structure with Pt.

Herein, we use an organometallic zero-valance Zn complex to incorporate hard-to-reduce Zn into Pt–*M* NPs by a facile wet method. The incorporation of Zn lowers the ordering temperature of Pt–*M*–Zn NPs in the formation of ordered IMC NPs, which suppresses sintering and leads to a high ordering degree. To improve ORR activity, i.e., to optimize the strain effect on the Pt outermost layer formed by acid treatment, compositionally controlled $L1_0$-type Pt(*M*,Zn) (*M* = Co or Ni) NPs with high ordering degree are synthesized through low-temperature annealing. The activity of the highly ordered $L1_0$-$Pt_5Co_4Zn_1$ and $L1_0$-$Pt_5Ni_4Zn_1$ NP catalysts is investigated under ORR conditions relevant to PEMFC s.

2. Experimental

2.1 Chemicals

Platinum(II) acetylacetonate ($Pt(acac)_2$, 97%), cobalt(III) acetylacetonate ($Co(acac)_3$, 98%), nickel(II) acetylacetonate ($Ni(acac)_2$, 95%), oleylamine (OAm, 80%–90%), borane–*tert*-butylamine complex (BBA, 97%), and Nafion (5% in a mixture of 2-propanol and water) were purchased from Sigma-Aldrich. Diphenylzinc (Ph_2Zn, 99%), *n*-hexane (98.5%), and ethanol (>99%) were purchased from Fujifilm Wako Pure Chemical. Ph_2Zn was dissolved in Oam to form a 10 mM solution and stored in an argon (Ar)-filled glovebox. Other chemicals were used without further purification.

2.2 Synthesis of *A*1-type Pt–*M*–Zn (*M* = Co, Ni) NPs

As a typical synthesis of *A*1-type $Pt_5Co_4Zn_1$ NPs, 0.05 mmol of $Pt(acac)_2$, 0.048 mmol of $Co(acac)_3$, 1.6 mL of 10 mM Ph_2Zn Oam solution, and 5.0 mL of Oam were mixed in a glass pressure tube in a glovebox under an inert reaction atmosphere. The reaction solution was heated with an oil bath at 80 °C for 30 min and then at 230 °C for 120 min, followed by cooling to room temperature. Next, 10 mL of *n*-hexane and 30 mL of ethanol were added to the reaction solution to precipitate the product. After centrifugation at 9000 rpm (9510 rcf) for 15 min and washing three times with a 1:4 volume ratio mixture of *n*-hexane and ethanol, *A*1-type $Pt_5Co_4Zn_1$ NPs were collected and dispersed in *n*-hexane for further use. By adjusting the feed ratio of $Co(acac)_3$, $Ni(acac)_2$, and Ph_2Zn, the compositions of *A*1-type Pt–*M*–Zn NPs were changed as desired. For the preparation of Pt_5Ni_5 NPs, 10 mg of BBA was added as a stronger reductant to decrease the NP size.[18]

2.3 Preparation of carbon-supported $L1_0$-Pt(*M*,Zn)@Pt NPs ($L1_0$-Pt(*M*,Zn)@Pt/C)

Carbon black (60 mg, Vulcan XC-72) was suspended in 60 mL *n*-hexane by sonication for 30 min and then an *n*-hexane dispersion of *A*1-type Pt–*M*–Zn NPs was added to this suspension. The loading amount of Pt was maintained at around 11 to 14 wt.%. After sonication for 1 h, the carbon-supported Pt–*M*–Zn NPs (Pt–*M*–Zn/C) were dried and annealed under 4% hydrogen (H_2) in Ar at a designated temperature (550 or 600 °C) to convert the *A*1 structure into $L1_0$ structure. $L1_0$-Pt(*M*,Zn)/C was then treated in 0.1 M $HClO_4$ aqueous solution at 60 °C for 12 h to give carbon-supported catalysts with $L1_0$-Pt(*M*,Zn)-Pt core–shell NPs ($L1_0$-Pt(*M*,Zn)@Pt/C) for further study. Disordered *A*1-PtCo@Pt/C and *A*1-PtNi@Pt/C catalysts for ORR testing were synthesized using identical procedures, followed by annealing at 400 °C to ensure uniform elemental distribution.

2.4 Thermogravimetric analysis (TGA) to measure Pt loading amount

TGA was conducted to measure the Pt loading amount of $L1_0$-Pt(*M*,Zn)@Pt/C. Before sample measurement, a blank TGA measurement was conducted using an empty pan under the same conditions as the sample measurement for background correction. The sample measurement was then conducted under 20% oxygen (O_2) in nitrogen (N_2) flowing at 300 mL/min. Temperature programming was set at 5 °C/min from 50 to 1000 °C to fully oxidize the carbon support. The residue consisted of Pt alloys. Background correction was performed by subtracting the thermogravimetric curve of the blank measurement from

that of the sample. The Pt mass loading of each sample was determined by combining TGA results with the sample composition determined by scanning electron microscopy–energy-dispersive X-ray spectroscopy (SEM-EDX).

2.5 Estimation of surface strain in $L1_0$-Pt(*M*,Zn)@Pt NPs

The surface strain in the Pt shell on the $L1_0$-Pt(*M*,Zn) core of the $L1_0$-Pt(M,Zn)@Pt NPs was estimated by comparison of the area of a triangle consisting of three neighboring atoms on {111} planes of $L1_0$-Pt(*M*,Zn) and that of pure Pt using the following equation to calculate the lattice mismatch strain.

$$Strain(\%) = \frac{S - S_{Pt}}{S_{Pt}} \quad (1)$$

where S and S_{Pt} represent the triangle areas of $L1_0$-Pt–*M*–Zn and pure Pt, respectively, as indicated in Figure S2. S and S_{Pt} were calculated from the lattice constant obtained by Rietveld refinement of the powder X-ray diffraction (XRD) pattern of $L1_0$-Pt–*M*–Zn and the literature value for the lattice constant of Pt (see Table S1), respectively.[10] A negative value of strain corresponds to compressive strain in the Pt shell.

2.6 Calculation of the long-range order parameter of $L1_0$-Pt(*M*,Zn) NPs

The average degree of chemical (atomic) order for ensemble $L1_0$-Pt(*M*,Zn) NPs can be evaluated as the long-range order parameter (S) extracted from the XRD pattern by comparing the integrated intensity ratio of the 110 superlattice reflection peak to the principal 111 reflection peak, I_{110}/I_{111}. The experimental I_{110}/I_{111} derived from the refined XRD pattern can be defined as:[21]

$$I_{110}/I_{111} = S^2\left(I^*_{110}/I^*_{111}\right) \quad (2)$$

where S is the LRO parameter and I^*_{110}/I^*_{111} is the simulated intensity ratio for the perfectly ordered $L1_0$-type intermetallic compound (IMC) with the ideal stoichiometric compositions of $Pt_{50}M_{50-x}Zn_x$. Thus, S values for perfectly ordered $L1_0$-Pt(*M*,Zn) and perfectly disordered *A*1-Pt(*M*,Zn) alloys are 1 and 0, respectively. To experimentally determine I_{110} and I_{111} with a high degree of accuracy, Rietveld refinement was performed in the 2ϑ range of 30° to 90° to avoid interference from the broad peak around 25° derived from the carbon support. The I^*_{110}/I^*_{111} ratio depends on the composition of $Pt_{50}M_{50-x}Zn_x$ to a non-negligible degree. Therefore, the I^*_{110}/I^*_{111} ratios of fully ordered alloys with corresponding compositions were simulated, as listed in Table S2.

2.7 Catalyst ink preparation and electrochemical measurements

Catalyst ink for electrochemical measurements was prepared by mixing carbon-supported catalyst (1 mg) with ultrapure water (800 μL), 2-propanol (200 μL), and Nafion solution (5 wt%, 10 μL) and sonicating the mixture for 1 h. Catalyst ink (10 μL) was then deposited on a glassy carbon rotating disk electrode (5 mm in diameter) and dried via a spin-assisted method at 700 rpm. The experiments were conducted in 0.1 M $HClO_4$ electrolyte using a three-electrode system with Pt wire as a counter electrode and a reversible hydrogen electrode (RHE, 5% H_2) as a reference electrode. The measured potential was corrected by adding 0.0385 V according to the Nernst equation. Cyclic voltammetry (CV) and linear sweep voltammetry (LSV) were used to evaluate catalytic performance. All potentials are referenced to RHE. Cleaning CV measurements were conducted by scanning the electrode in the range of 0.02–1.20 V at 100 mV/s for 50 cycles under N_2 saturation. The final CV was collected in the range of 0.02–1.10 V at 50 mV/s to calculate the electrochemical surface area (ECSA) from the H_{upd} adsorption peak area of the final CV. LSV of the ORR was conducted by positively scanning from 0.2 to 1.2 V at 10 mV/s during rotation at 2500 to 100 rpm in an O_2-saturated atmosphere. The final ORR linear scanning current was corrected by subtracting the current obtained in N_2-saturated atmosphere using the same method and conditions. The specific activity (i_s) and mass activity (i_m) at 0.9 V (vs. RHE) were calculated based on the Koutecky‑Levich equation. Accelerated durability tests (ADTs) were conducted in a half-cell configuration using constant-potential polarization at 0.60 and 0.95 V (3 s at each potential). After every 2,500 cycles, cyclic voltammograms (CVs) were recorded to evaluate the ECSA of the catalysts.

2.8 Material characterization

The SEM-EDX measurements were performed using an Edax Apollo XF attachment on a scanning electron microscope (SEM, Hitachi S-4800) at 20 kV, which detected Co-K, Ni-K, Zn-K, and Pt-L peaks. XRD patterns were collected at room temperature using a powder diffractometer in Bragg–Brentano configuration (Malvern Panalytical Aeris) with Cu Kα radiation (λ = 1.542 Å) at 40 kV and 15 mA. Rietveld refinements were performed using HighScore Plus, which is the commercial powder diffraction analysis software from Malvern Panalytical.[22] Magnetic hysteresis *M*–*H* loops were measured on a superconducting quantum interface device (Quantum Design MPMS3) with a field of up to 7 T. Transmission electron microscopy (TEM) images were obtained on a transmission electron microscope (HT7820, Hitachi) at an accelerating voltage of 120 kV. High-resolution transmission electron microscopy (HRTEM), high-angle annular dark field-scanning transmission electron microscopy (HAADF-STEM), EDX spectroscopy, and electron energy loss spectroscopy (EELS) were conducted with a transmission electron microscope (JEM-ARM200F, JEOL) at an accelerating voltage of 200 kV.

2.9 Computational calculations

Density functional theory (DFT) calculations were performed on $L1_0$-Pt_1M_1 (*M* = Fe, Co, Ni, Zn) and Zn-doped $L1_0$-$Pt_1M_{0.5}Zn_{0.5}$ (*M* = Fe, Co, Ni) systems using the OpenMX code.[23] The generalized gradient approximation of Perdew–Burke–Ernzerhof was employed for the exchange-correlation functional, and pseudo-atomic orbital basis sets (*s*3*p*2*d*1 for Fe, Co, Ni, and *s*3*p*2*d*2*f*1 for Pt) were used. Cutoff radii were set to 6.0 a.u. for Fe, Co, Ni, and 9.0 a.u. for Pt, with a cutoff energy of 500 Ry. A *k*-point mesh of 23×23×17 was used for Zn-doped $L1_0$-$Pt_1M_{0.5}Zn_{0.5}$ systems and one of 16×16×17 was used for the other systems. Conventional

View Article Online DOI: 10.1039/D5TA08256K

cells were chosen as 1×1×1 for $L1_0$-Pt_1M_1 systems and √2×√2×1 for Zn-doped $L1_0$-$Pt_1M_{0.5}Zn_{0.5}$ systems to accommodate for different atomic positions. The formation energies E_{form} of $L1_0$-Pt_1M_1 and $L1_0$-$Pt_2M_1Zn_1$ were calculated using the following equation.

$$E_{form} = E_{alloy} - (\alpha \times \mu[Pt] + \beta \times \mu[M]) \quad (3)$$

where E_{alloy} is the total energy of the alloys; μ[Pt] and μ[*M*] are the chemical potentials of Pt and *M*, respectively, which are equivalent to the total energies of these ground states; and α and β are integers.

To investigate the effects of Zn addition on $L1_0$-Pt*M* (*M* = Fe, Co, Ni) and its structural stability, E_{form} calculations were performed for systems where Zn was added to $L1_0$-Pt*M* and *A*1-Pt*M*. The generation of structures with different Zn concentrations was accomplished using special quasirandom structures (SQS), which can consider randomness with high accuracy.[24] The generated structures were constructed using a 2×2×2 supercell of the $L1_0$ structure, which contained a total of 32 atoms: 16 Pt atoms and either *M* or Zn atoms (16 in total). In the *A*1 structure, the randomness of all elements was considered, whereas in the $L1_0$ structure, only the positions of the Pt atoms were fixed, allowing for substitutions of *M* atoms and Zn. For each Zn concentration *x*, all structures generated by SQS were selected, with a constant Pt concentration. E_{form} calculations were conducted using Matlantis v.7.0.0, a versatile atomistic simulator that implements neural network potentials.[25] By performing structural optimizations on all model structures generated by SQS, the total energy of the systems was obtained. Subsequently, E_{form} for each system was calculated.

3. Results and discussion

3.1 Synthesis of highly ordered alloy $L1_0$-Pt(*M*,Zn)@Pt/C

Considering that $L1_0$-PtZn possesses a much lower T_{PT} than those of other $L1_0$-Pt*M* alloy NPs, we envisioned that Zn would promote ordering in the transformation of *A*1 to $L1_0$ structure at relatively low temperature to achieve both a high degree of ordering and sintering suppression. However, incorporation of hard-to-reduce Zn into nanosized Pt*M* alloy with ideal composition and monodispersity is challenging because of the large negative standard electrode potential of Zn^{2+}/Zn ($E°$ at 25 °C = −0.76 V). Synthesis of PtZn IMC NPs usually involves the reduction of Zn^{2+} in Pt/Zn^{2+} nanocomposites, such as Pt NPs encapsulated in a ZnO matrix,[8] Pt NPs surrounded by zeolitic imidazolate frameworks containing Zn^{2+},[20] Pt NPs coated with a thin ZnO shell,[26] and Zn-covered Pt NPs obtained by Zn vapor deposition.[27] The high reaction temperature and complicated procedures in these strategies make it difficult to properly manipulate the composition and morphology of PtZn IMC NPs.

Here, we used an organometallic zero-valance Zn complex to incorporate difficult-to-reduce Zn into Pt–*M* NPs by a facile wet chemical process to synthesize monodisperse Pt–*M*–Zn NPs. Zero-valent organozinc enables mild and well-controlled incorporation of Zn, suppressing independent Zn nucleation and promoting homogeneous alloying, which leads to uniform nanoparticle morphology and composition. The overall synthesis of carbon-supported $L1_0$-type Pt(*M*,Zn)-Pt core–shell NPs (denoted as $L1_0$-Pt(*M*,Zn)@Pt/C) is schematically represented in Figure 1. First, platinum(II) bis(acetylacetonate) ($Pt(acac)_2$), cobalt(III) Tris(acetylacetonato) ($Co(acac)_3$), Nickle(II) bis(acetylacetonate) ($Ni(acac)_2$), Diphenylzinc (Ph_2Zn) with specified molar ratios were co-reduced in oleylamine (OAm). Ph_2Zn with zero-valance state Zn was used to directly incorporate Zn into the Pt*M* alloys to avoid the Zn^{2+} reduction procedure. The synthesized *A*1-type (i.e., face-centered cubic (fcc)-based solid solution) Pt–*M*–Zn NPs were supported on carbon (denoted as *A*1-Pt–*M*–Zn/C) and then transformed into highly ordered $L1_0$ structure by low-temperature reductive annealing (denoted as $L1_0$-Pt(*M*,Zn)/C), followed by acid post-treatment to generate a Pt shell on the NP surface ($L1_0$-Pt(*M*,Zn)@Pt/C).

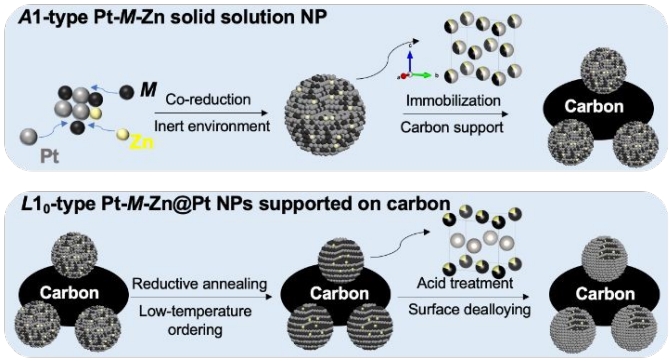

Fig. 1 Synthesis of $L1_0$-type Pt(*M*,Zn)@Pt NPs supported on carbon.

3.2 Precise composition control and phase transformation of *A*1-Pt–*M*–Zn NPs

Figure 2A–F and S4A,B show transmission electron microscopy (TEM) images of the as-synthesized Pt–*M*–Zn NPs and corresponding size distributions. The average sizes of the monodisperse Pt–*M*–Zn NPs determined by measuring 200 randomly selected NPs for each sample were 3.5–6.5 nm, which matched well with X-ray diffraction (XRD) results (Table S3). The particle size decreased with increasing Zn content in both *M* cases because of highly active Ph_2Zn.[28] Based on the theory that too large or too small particle size is not suitable in terms of electrochemically active surface area (ECSA) or ordering from *A*1 to $L1_0$ structure during annealing, respectively, the optimal NP size is empirically considered to be in the 4–6-nm range. For the specific stoichiometry required for $L1_0$ structure formation, we controlled the atomic ratio of Pt/nonprecious metal in the NPs to be around 1:1 (Table S4). The XRD patterns of a series of as-synthesized Pt–*M*–Zn/C are presented in Figure 2G. The diffraction peaks indicate that their crystal structures are fcc, meaning that the Pt–*M*–Zn NPs possess *A*1 structure with disordered distributions of all elements. The diffraction peaks shift to lower angle with increasing Zn/*M* ratio.

The as-synthesized *A*1-type NPs uniformly distributed on carbon supports were subjected to reductive annealing to induce phase transformation. The loading amount of Pt was controlled in the range

Journal Name ARTICLE

View Article Online
DOI: 10.1039/D5TA08256K

of 11–15 wt.%, as confirmed by thermogravimetric analysis (see Table S4). Although ordering of Pt*M* NPs at high temperature is usually accompanied by sintering,[29] severe sintering was not observed for *A*1-Pt–*M*–Zn/C annealed at 600 and 550 °C (see Figure S5 and S6, respectively). XRD patterns of annealed samples (Figure 3A,B,D, and E) contained symmetric and broad diffraction peaks, indicating no severe aggregation, and new clear superlattice peaks at 33° (assignable to 110 peaks) demonstrating the formation of the $L1_0$ structure. As expected from calculations, we observed splitting of the 200 peaks of fcc structure into 200 and 002 peaks of $L1_0$ structure with shifts of the 200 peak to lower angle and 002 peak to higher angle with increasing Zn content. These changes indicated longer

Fig. 2 Characterization of *A*1-Pt(*M*,Zn)/C NPs. TEM images, elemental compositions (at.%), and size distributions (inset) of as-synthesized (A) *A*1-Co_5Pt_5, (B) *A*1-$Pt_5Co_4Zn_1$, (C) *A*1-$Pt_5Co_{2.5}Zn_{2.5}$, (D) *A*1-Ni_5Pt_5, (E) *A*1-$Pt_5Ni_4Zn_1$, and (F) *A*1-$Pt_5Ni_{2.5}Zn_{2.5}$ NPs.(G, H) XRD patterns of *A*1-Pt(*M*,Zn)/C before reductive annealing. The broad peak at around 25° was ascribed to the carbon support.

lattice constants along <100> directions (a and b) and shorter lattice constants along <001> directions (c) after annealing; that is, tetragonality (a/c) increased, consistent with the formation of $L1_0$ structure. Element distributions in $L1_0$-Pt(Co,Zn) and $L1_0$-Pt(Ni,Zn) were further analyzed by high-angle annular dark field scanning transmission electron microscopy (HAADF-STEM) and energy-dispersive X-ray spectroscopy (EDS) mapping. Uniform distributions of three elements in individual NPs were observed for both $L1_0$-Pt(Co,Zn) and $L1_0$-Pt(Ni,Zn) NPs, indicating no phase segregation after reductive annealing with or without subsequent acid treatment (Figure 3C and F and S7–S11). These results strongly confirmed that the disordered *A*1 structure of the as-synthesized NPs with various

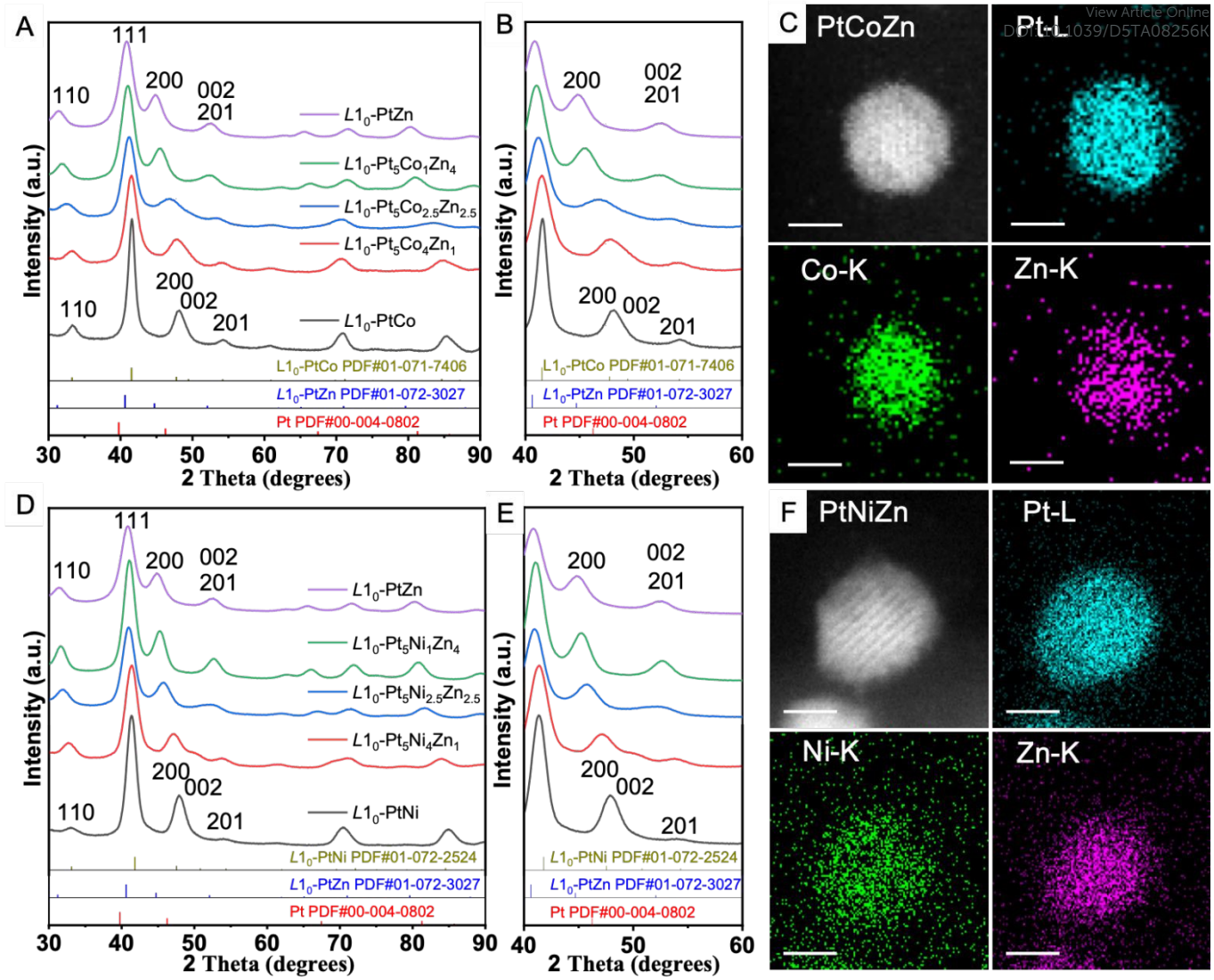

Fig. 3 Characterization of $L1_0$-Pt(*M*,Zn)/C NPs. (A, B) XRD patterns of $L1_0$-Pt(Co,Zn)/C. (C) STEM image and corresponding elemental mapping images of a single $L1_0$-$Pt_5Co_{2.5}Zn_{2.5}$ NP. (D, E) XRD patterns of $L1_0$-Pt(Ni,Zn)/C NPs. (F) STEM image and corresponding elemental mapping images of a single $L1_0$- $Pt_5Ni_{2.5}Zn_{2.5}$ NP (Pt: blue, Co or Ni: green, Zn: purple).

Zn/M ratios was converted to ordered $L1_0$ structure by reductive annealing.

3.3 Zn-promoted formation of highly ordered $L1_0$-Pt(*M*,Zn) NPs

S is a critical parameter that determines both the activity and durability of catalysts. *S* of the NPs was evaluated by calculating the integrated intensity ratio I_{110}/I_{111} obtained from the Rietveld refinement of XRD data (see Figure S12 and S13 and Methods in the SI).[30, 31] $L1_0$-Pt_5Co_5/C and $L1_0$-Pt_5Ni_5/C obtained by reductive annealing for 6 h at 600 and 550 °C, respectively, showed *S* of 65% and 47%, respectively. $L1_0$-$Pt_5Co_4Zn_1$/C and $L1_0$-$Pt_5Ni_4Zn_1$/C obtained under the same conditions possessed higher *S* of 78% and 81%, respectively, which was induced by the small amount of Zn. When the annealing temperature of *A*1-Pt_5Co_5/C was increased from 600 to 650 °C, *S* of the resulting $L1_0$-Pt_5Co_5/C reached 79%, although obvious sintering took place in areas with high NP density (Figure S14). Different from $L1_0$-Pt_5Co_5/C, *S* of $L1_0$-Pt_5Ni_5/C obtained by annealing *A*1-Pt_5Ni_5/C at 600 °C was 36%, probably because of the low T_{PT} of PtNi of ~630 °C (Figure S15). These results demonstrate that the initiation of ordering at lower relative temperature in the presence of Zn is effective for obtaining highly ordered $L1_0$-Pt(*M*,Zn)/C. The *S* values of $L1_0$-Pt(Co,Zn)/C and $L1_0$-Pt(Ni,Zn)/C obtained at various annealing temperatures are summarized in Table S5. These values clearly show that *S* was increased by the presence of Zn even for small NPs. To study the effect of NP size on *S* without Zn incorporation, $L1_0$-Pt_5Co_5/C and $L1_0$-Pt_5Ni_5/C with a size of around 5 nm were also synthesized. These samples exhibited lower *S* than their larger counterparts (Figure

View Article Online
DOI: 10.1039/D5TA08256K

S16 and S17 and Table S5). These results further emphasize the importance of Zn incorporation for achieving high *S* in small NPs.

To consider the origin of the increase of *S* achieved by the addition of Zn, the formation energies (E_{form}) of *A*1- and $L1_0$-Pt(*M*,Zn) with various compositions were estimated by theoretical calculations. Calculated E_{form} of binary Pt*M* at 0 K are more negative in the order PtCo < PtNi < PtFe < PtZn for both *A*1 and $L1_0$ structures (Figure S18 and S19). The $L1_0$ structure is the thermodynamically stable phase with larger E_{form} than the *A*1 structure for all Pt*M* in the low temperature region. The difference between E_{form} of the *A*1 and $L1_0$ structures ($\Delta E_{form} = E_{form}[A1] - E_{form}[L1_0]$) of each Pt*M* is shown in Figure S19B. ΔE_{form} is an indicator of the difficulty of phase transformation from $L1_0$ to *A*1 at high temperature. A larger positive value of ΔE_{form} indicates that the phase transformation can occur at higher temperature. ΔE_{form} increased in the order PtNi < PtCo < PtFe < PtZn, corresponding to the ascending order of T_{PT} obtained from bulk Pt–*M* binary phase diagrams (T_{PT}: PtNi ~630 °C < PtCo ~820 °C < PtFe ~1300 °C, PtZn over 900 °C [data over 900 °C are not available]). ΔE_{form} of $Pt_1M_{1-x}Zn_x$ with various compositions ($0 < x < 1$) are summarized in Figure S19. The tendency of ΔE_{form} to increase with Zn content in all systems strongly suggests that the incorporation of Zn contributes to the increase of T_{PT} by making the $L1_0$ structure more stable than the *A*1 structure with the same composition, resulting in the promotion of $L1_0$ ordering even for small NPs.

The high degree of ordering induced by the introduction of Zn was further confirmed by magnetic measurements, as shown in Figure S20. $L1_0$-Pt_5Co_5, $Pt_5Co_4Zn_1$, and $Pt_5Co_{2.5}Zn_{2.5}$ obtained by reductive annealing at 600 °C for 6 h exhibited superparamagnetic behavior at 27 °C and almost no coercivity (H_c), which could be explained by the low blocking temperature caused by their small NP size.[32] Magnetic hysteresis loops were then measured at –263 °C. $L1_0$-Pt_5Co_5 showed hard magnetic properties with low H_c (2.6 kOe) and high saturation magnetization. In contrast, both $L1_0$-$Pt_5Co_4Zn_1$ and $L1_0$-$Pt_5Co_{2.5}Zn_{2.5}$ exhibited harder magnetic properties with higher H_c of 10.0 and 12.0 kOe, respectively, and lower saturation magnetization.[33] This change in magnetic properties induced by Zn substitution could be explained by the increase in H_c caused by the increase in magnetic anisotropy resulting from the increase in the tetragonality of the $L1_0$ structure (see Table S5) and the decrease in magnetization caused by the decreased content of 3*d* lone-pair electrons. The approximately single-phase loops of $L1_0$-$Pt_5Co_4Zn_1$ and $L1_0$-$Pt_5Co_{2.5}Zn_{2.5}$ also indicate the uniform distribution of Zn atoms at an atomic level in the NPs. These results confirmed that Zn incorporation promoted atom diffusion at lower temperature, resulting in the formation of $L1_0$ structures with high *S*.[34]

3.4 Formation of compressed Pt-Rich shells on $L1_0$-Pt(*M*,Zn) cores

To use the series of $L1_0$-Pt(*M*,Zn)/C as ORR catalysts, the samples were first subjected to acid treatment to generate Pt-rich shells through the etching of *M* from the NP surface. Elemental compositions before and after acid treatment were analyzed by SEM-EDX, from which it was confirmed that around 50% of *M* remained in the ordered $L1_0$ NPs (Table S4). Contrary to the ordered $L1_0$ NPs, dramatic decreases of *M* content were observed in disordered *A*1-Pt*M* NPs (PtNi: 48% to 18%, PtCo: 50% to 32%) after acid treatment, indicating the superior resistance of the ordered alloy structure towards *M* etching.

Detailed structural analysis of $L1_0$-Pt(*M*,Zn)@Pt NPs was conducted by HAADF-STEM and EDS mapping (Figure 4, S7, and S8). Figure 4A shows an HAADF-STEM image of a typical $L1_0$-$Pt_5Co_{2.5}Zn_{2.5}$ NP enclosed by major {111} and {001} facets and^^ minor {110} facets. The NP consists of a thin Pt shell and intermetallic $L1_0$ core of alternating Pt and Co/Zn columns, represented by dots with brighter and darker contrast, respectively. Note that it is difficult to distinguish Zn from Co and Ni in the HAADF-STEM image because of their similar *Z* contrast. Figure 4B presents the fast Fourier transform (FFT) image of Figure 4A, which shows superlattice spots such as 001 and 1−10 characteristic of $L1_0$ structure. The interplanar spacing of {001} planes (*d*{001}) measured from the masked inverse FFT image was 0.372 nm (Figure 4C), which agreed well with the lattice constant c of $L1_0$-$Pt_5Co_{2.5}Zn_{2.5}$ NPs determined from XRD refinement. The $L1_0$ structure core was further verified by the elemental mapping images (Figure 4E–I), which showed alternating layers of Pt and Co/Zn. The acid treatment of $L1_0$-$Pt_5Co_{2.5}Zn_{2.5}$ at 60 °C for 10 h provided a Pt-rich shell with a thickness of two to three atomic layers, as clearly seen in EDS line-scanning profiles (Figure 4J and K), HAADF-STEM *Z*-contrast profiles (Figure 4L and M), and electron energy loss spectroscopy mapping images (Figure S21). XRD patterns before and after the acid treatment of representative $L1_0$-$Pt_5Co_{2.5}Zn_{2.5}$/C (Figure S22) further confirmed the formation of core–shell structure. That is, no shift of the superlattice peaks was observed after acid treatment, indicating the $L1_0$ structure was robust. The small negative shift of the non-superlattice peaks was caused by the etching of *M* to form the shell structure.

To experimentally confirm the compressive strain in the Pt-rich shell, we measured the actual interatomic distances in the Pt-rich shell from the HAADF-STEM *Z*-contrast image in Figure 4A (also see Figure S23 and S24). The interatomic distance between neighboring atoms in the {001} planes projected from the <110> direction corresponds to *d*{110}. The average measured *d*{110} values in the surface atomic layers were 0.266, 0.261, and 0.266 nm for the first, second, and third layer, respectively, which are considerably shorter than *d*{110} of both pure Pt (0.277 nm), despite the Pt-rich composition, and the highly ordered alloy core (0.271 nm). A similar trend was observed for the {111} plane. These results strongly support that the Pt-rich shells are subjected to compressive strain induced by the smaller lattice of the $L1_0$-PtM core relative to that of the shell. However, because it is complicated to determine the average compressive surface strain of a sample macroscopically, the surface strain of Pt shells (see the Methods section in the SI for definition) was estimated by calculating the lattice mismatch between $L1_0$-Pt(*M*,Zn) and pure Pt from the average lattice constant determined macroscopically by XRD measurements. The calculation results plotted in Figure S3 showed that higher Zn content leads to lower surface strain. This is logical because the atomic radius of Zn (134 pm) is larger than those of Co (125 pm) and Ni (125 pm).

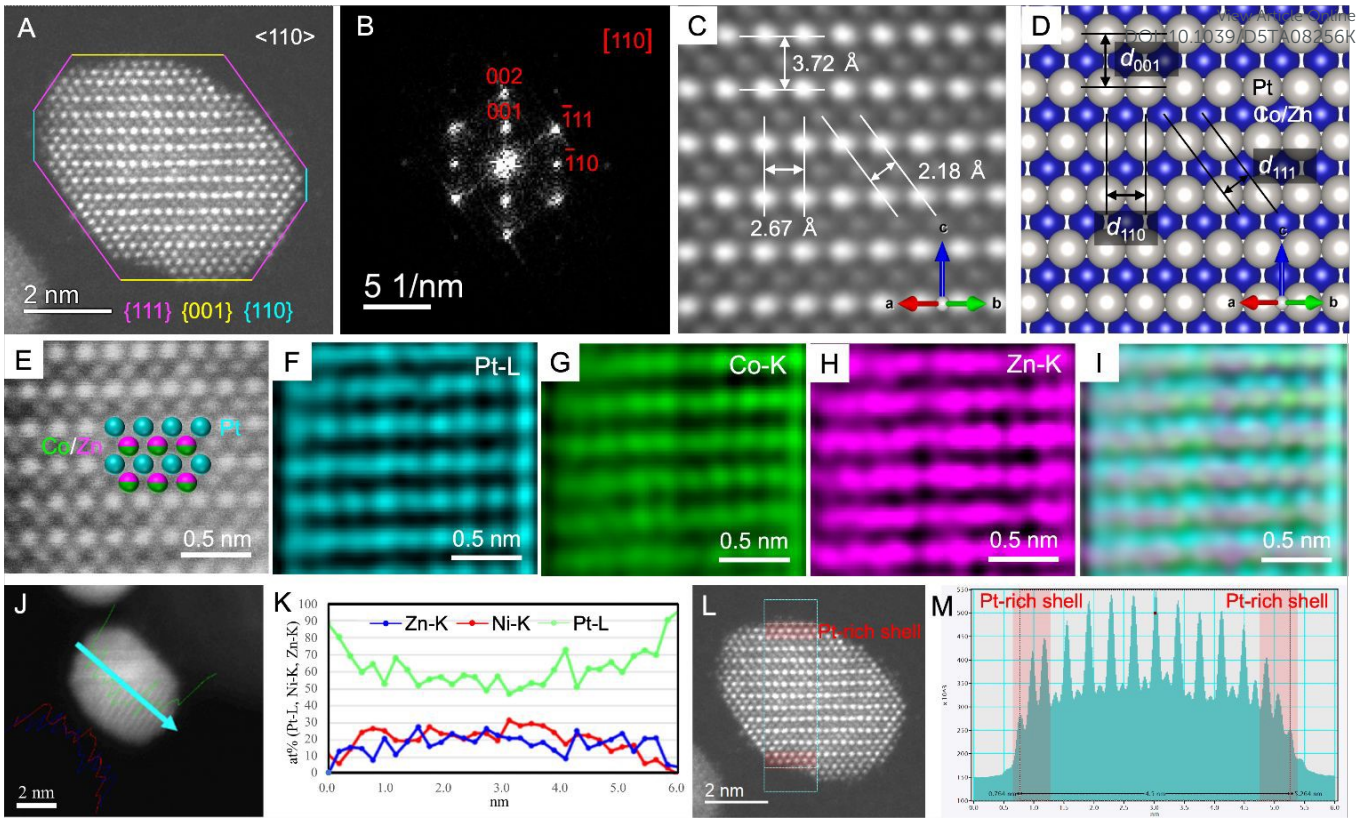

Fig. 4 Structural analyses of a single $L1_0$-$Pt_5Co_{2.5}Zn_{2.5}$@Pt NP. (A) HAADF-STEM image, (B) FFT image of (A) (zone axis is the <110> direction), (C) masked inverse FFT image of (B), and (D) schematic model of $L1_0$-Pt*M* along the <110> direction (Pt: gray, M: blue) corresponding to (C). (E–I) High-resolution STEM elemental mapping images after passing through a Wiener filter, (J) HAADF image, (K) EDS line-scan profiles showing the distributions of Pt, Ni, and Zn, (L) HAADF- STEM *Z*-contrast image, and (M) *Z*-contrast profile from the indicated area in (L).

However, the incorporation of low content of Zn can still lead to high *S* and large compressive surface strain.

Overall, acid treatment provided NPs with $L1_0$-Pt(*M*,Zn)@Pt core–shell structure by the effective etching of *M*/Zn components from the $L1_0$-Pt(*M*,Zn) NP surface. The Pt shells showed compressive strain caused by the lattice mismatch between the Pt shells and $L1_0$ cores, which is promising for achieving simultaneous improvements of ORR durability and activity.

3.5 ORR electrocatalytic performance of highly ordered $L1_0$-Pt(*M*,Zn)@Pt/C

The electrocatalytic performance of highly ordered $L1_0$-Pt(*M*,Zn)@Pt/C in the acidic ORR was evaluated using a typical thin-film rotating disc electrode technique. Cyclic voltammetry (CV) measurements were conducted in N_2-saturated 0.1 M $HClO_4$ aqueous solution at room temperature until stable CV curves were obtained (Figure 5A and D). ECSA of the samples was calculated from the charge of hydrogen underpotential deposition and normalized by the Pt loading mass (see the SI for details). The ECSA values of $L1_0$-Pt(*M*,Zn)@Pt/C (40–60 m^2/g_{Pt}) and commercial standard Pt/C (67 m^2/g_{Pt}) tended to increase with decreasing NP size (Table S6). The surface areas of $L1_0$-Pt(*M*,Zn)@Pt/C are much higher than those of recently reported Pt*M* IMCs catalysts because of the smaller initial particle size with narrower distribution and their morphology retention without aggregation after low-temperature annealing. [6, 7, 9, 15]

After obtaining stable CV curves, linear sweep voltammetry (LSV) was used to study the ORR catalytic activity of the highly ordered catalysts. As examples, the LSV polarization curves measured in O_2-saturated 0.1 M $HClO_4$ aqueous solution at 1600 rpm are shown in Figure 5B and E. In both $L1_0$-Pt(Co,Zn)@Pt and $L1_0$-Pt(Ni,Zn)@Pt systems, the half-wave potential increased with the amount of Co or Ni. Specific activity (i_s) and mass activity (i_m) at 0.9 V vs. RHE were calculated from kinetically controlled current (i_k) and ECSA (Figure 5C and F), where i_k was obtained from Koutecky–Levich plots of current extracted from LSVs measured at various rotation rates. The

View Article Online
DOI: 10.1039/D5TA08256K

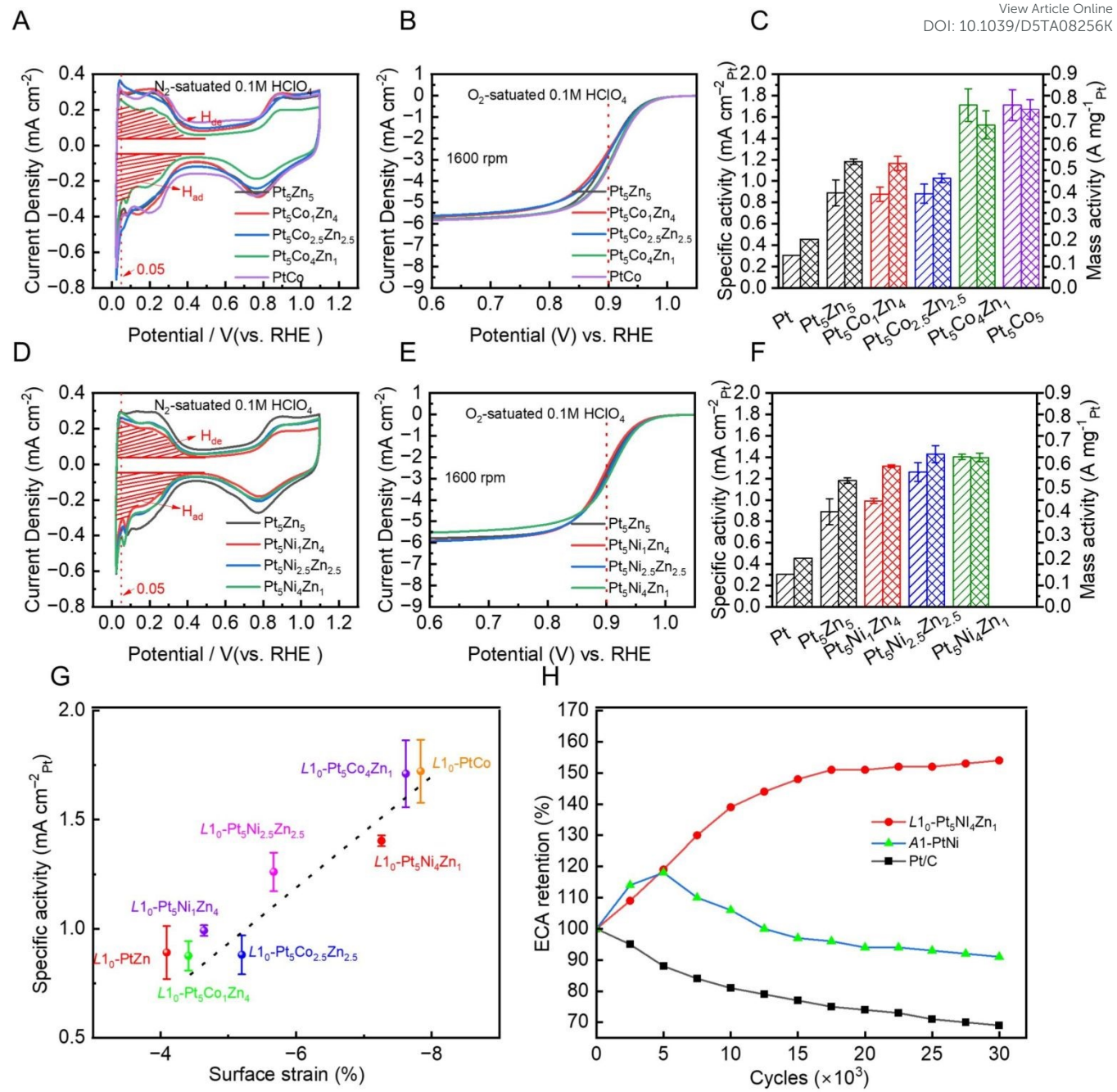

Fig. 5 Electrochemical catalytic activities of L10-Pt(M,Zn)@Pt/C. (A, D) CV curves, (B, E) ORR polarization curves at 1600 rpm, and (C, F) specific and mass activities at 0.9 V vs. SHE of highly ordered (S >70%) (A–C) $L1_0$-Pt(Co,Zn)@Pt/C and (D–F) $L1_0$-Pt(Ni,Zn)@Pt/C. (G) Correlation between specific activity and calculated surface strain of Pt shells. (H) ECSA retention of the catalysts during the ADT cycles in the RDE test.

highest catalytic activity among the series of ternary $L1_0$-Pt(*M*,Zn)@Pt/C was obtained for $L1_0$-$Pt_5Co_4Zn_1$@Pt/C, which showed i_s of 1.71 mA/cm$^2_{Pt}$ and i_m of 0.69 A/mg$_{Pt}$. These values are comparable with those of binary $L1_0$-Pt_5Co_5@Pt/C and are approximately 5.6 and 3.3 times higher than those of commercial Pt/C, respectively.

To quantitatively discuss the effect of compressive strain in Pt-rich shells on ORR catalytic activity, the surface strain of each highly ordered sample with S > 0.7, which was estimated from the lattice mismatch of the ORR-active {111} facets shown in Figure S3, was plotted against i_s (Figure 5G). This plot showed the monotonic increase of i_s with compressive surface strain. Therefore, the high ORR activity of $L1_0$-Pt(*M*,Zn)@Pt/C likely results from the high compressive strain in the Pt-rich shell with a thickness of two to three atomic layers derived from the smaller atomic radius of Co/Ni compared to that of Zn. The compressive strain induced in {111} planes is believed to modify the electronic structure, causing a downward shift of the *d*-band centre. This shift reduces the binding

View Article Online
DOI: 10.1039/D5TA08256K

energy of oxygen intermediates and kinetically enhances ORR activity.[35-38] In contrast, the poorly ordered $L1_0$-PtNi (~38%) exhibits a significantly lower ECSA (25 m^2Pt/g_{Pt}) and specific activity (0.491 mA/cm^2_{Pt}) compared with the highly ordered $L1_0$-Pt(*M*,Zn) counterparts (Table S6). The inferior ORR performance of $L1_0$-PtNi can be primarily attributed to its low degree of ordering, which restricts the beneficial strain and structural effects associated with ordered intermetallic phases. These results suggest that dealloying by *M* leaching and coarsening by agglomeration and Ostwald ripening of NPs during electrochemical cleaning processes prior to activity evaluation decrease activity and ECSA;[39] that is, the high *S* of $L1_0$-Pt(*M*,Zn)@Pt/C contributes the improvement of both catalytic activity and durability.

To further confirm the exceptional durability of the highly ordered $L1_0$-Pt(*M*,Zn)@Pt/C, accelerated durability tests (ADTs) were performed on Pt/C, *A*1-PtNi@Pt/C, and the representative $L1_0$-$Pt_5Ni_4Zn_1$@Pt/C in a half-cell configuration for comparison. The ECSA retention as a function of cycle number revealed a continuous decline for commercial Pt/C, retaining only ~69% after 30,000 cycles (Figure 5H). In contrast, both $L1_0$-$Pt_5Ni_4Zn_1$@Pt/C and disordered *A*1-PtNi@Pt/C exhibited an initial increase in ECSA during the early stages of ADT. This phenomenon is generally attributed to electrochemical surface activation, including selective dissolution of less noble metals and surface reconstruction, which exposes previously inaccessible Pt active sites.[40-42] With continued cycling, the disordered *A*1-PtNi@Pt/C catalyst experienced rapid ECSA decay following the initial activation, indicative of accelerated Ni leaching and structural degradation. Conversely, the highly ordered $L1_0$-$Pt_5Ni_4Zn_1$@Pt/C maintained a sustained increase in ECSA throughout the ADT, suggesting that atomic ordering effectively suppresses excessive metal dissolution while enabling controlled surface activation. These findings are corroborated by TEM images before and after ADT (Figure S26), which revealed significant particle growth for Pt/C and *A*1-PtNi@Pt/C, whereas the particle size of $L1_0$-$Pt_5Ni_4Zn_1$@Pt/C remained essentially unchanged. These observations underscore the superior structural stability of the ordered intermetallic catalyst under prolonged cycling conditions.

4. Conclusions

A feasible strategy to synthesize highly ordered IMC NPs with well-defined structures and compositions was developed. The ordering degree of $L1_0$-Pt*M* NPs was increased and aggregation was prevented by Zn incorporation at low temperature. The ordering degree was greatly improved while maintaining a strain effect by decreasing the amount of Zn, which gave high ORR specific activity under harsh electrochemical conditions. In particular, $L1_0$-$Pt_5Co_4Zn_1$ showed a mass activity of 0.69 A/mg_{Pt} and specific activity of 1.71 mA/cm^2_{Pt}, demonstrating its potential for fuel-cell applications. By precisely controlling NP composition, a comprehensive map of the correlation between the strain effect and ORR activity was constructed, which showed that specific activity increases monotonically with the compressive strain of surface Pt. These results provide us with insight into the tuning of ORR catalytic activity by finely controlling the structures of IMC NPs.

Author contributions

W.T., R.S., T.T. conceived the study. W.T., R.S. designed the synthesis scheme. W.T. performed the synthesis. W.T., R.S., K.M. were responsible for the characterization. W.T., R.S., T.U., Y.U. measured the electochemical catalytic properties. W.T., R.S. collected and analyzed the HAADF-STEM images and EDX elemental maps. Y.T. performed theoretical calculations. W.T., R.S., T.T. co-wrote the manuscript. All authors discussed the results and commented on the manuscript.

Conflicts of interest

There are no conflicts to declare.

Data availability

The data that support the findings of this study are available from the corresponding author upon reasonable request.
Supplementary information: supplementary figures (Figs. S1–S25) and tables (Tables S1–S7) (PDF). See DOI: See DOI: https://doi.org/XXX/XXX

Acknowledgements

The PEMFC project commissioned by the New Energy and Industrial Technology Development Organization (NEDO) (Grant No. 20001199-0 [T.T.]). Japan Science and Technology Agency, Core Research for Evolutionary Science and Technology (JST-CREST) (Grant No. JPMJCR21B4 [T.T.]). The Japan Society for the Promotion of Science (JSPS) KAKENHI for Scientific Research (S) (Grant No. JP24H00053 [T.T.]) and Scientific Research (B) (Grant No. JP23K26627 [R.S.]). High-resolution STEM analyses were performed under the NEDO FC-Platform. We thank Natasha Lundin, PhD, from Edanz (https://jp.edanz.com/ac) for editing a draft of this manuscript.

References

1. R. Borup, J. Meyers, B. Pivovar, Y. S. Kim, R. Mukundan, N. Garland, D. Myers, M. Wilson, F. Garzon, D. Wood, P. Zelenay, K. More, K. Stroh, T. Zawodzinski, J. Boncella, J. E. McGrath, M. Inaba, K. Miyatake, M. Hori, K. Ota, Z. Ogumi, S. Miyata, A. Nishikata, Z. Siroma, Y. Uchimoto, K. Yasuda, K.-i. Kimijima and N. Iwashita, *Chem. Rev.*, 2007, **107**, 3904–3951.
2. J. K. Nørskov, J. Rossmeisl, A. Logadottir, L. Lindqvist, J. R. Kitchin, T. Bligaard and H. Jónsson, *J. Phys. Chem. B*, 2004, **108**, 17886–17892.
3. C. Chen, Y. Kang, Z. Huo, Z. Zhu, W. Huang, H. L. Xin, J. D. Snyder, D. Li, J. A. Herron, M. Mavrikakis, M. Chi, K. L. More, Y. Li, N. M. Markovic, G. A. Somorjai, P. Yang and V. R. Stamenkovic, *Science*, 2014, **343**, 1339–1343.

4. X. Tian, X. Zhao, Y.-Q. Su, L. Wang, H. Wang, D. Dang, B. Chi, H. Liu, E. J. M. Hensen, X. W. Lou and B. Y. Xia, *Science*, 2019, **366**, 850–856.
5. D. Wang, H. L. Xin, R. Hovden, H. Wang, Y. Yu, D. A. Muller, F. J. DiSalvo and H. D. Abruña, *Nat. Mater.*, 2013, **12**, 81–87.
6. J. Li, S. Sharma, X. Liu, Y.-T. Pan, J. S. Spendelow, M. Chi, Y. Jia, P. Zhang, D. A. Cullen, Z. Xi, H. Lin, Z. Yin, B. Shen, M. Muzzio, C. Yu, Y. S. Kim, A. A. Peterson, K. L. More, H. Zhu and S. Sun, *Joule*, 2019, **3**, 124–135.
7. J. Li, Z. Xi, Y. T. Pan, J. S. Spendelow, P. N. Duchesne, D. Su, Q. Li, C. Yu, Z. Yin, B. Shen, Y. S. Kim, P. Zhang and S. Sun, *J. Am. Chem. Soc.*, 2018, **140**, 2926–2932.
8. J. Liang, Z. Zhao, N. Li, X. Wang, S. Li, X. Liu, T. Wang, G. Lu, D. Wang, B.-J. Hwang, Y. Huang, D. Su and Q. Li, *Adv. Energy Mater.*, 2020, **10**, 2000179.
9. W. J. Zeng, C. Wang, Q. Q. Yan, P. Yin, L. Tong and H. W. Liang, *Nat. Commun.*, 2022, **13**, 7654.
10. T.-W. Song, C. Xu, Z.-T. Sheng, H.-K. Yan, L. Tong, J. Liu, W.-J. Zeng, L.-J. Zuo, P. Yin, M. Zuo, S.-Q. Chu, P. Chen and H.-W. Liang, *Nat. Commun.*, 2022, **13**, 6521.
11. C.-L. Yang, L.-N. Wang, P. Yin, J. Liu, M.-X. Chen, Q.-Q. Yan, Z.-S. Wang, S.-L. Xu, S.-Q. Chu, C. Cui, H. Ju, J. Zhu, Y. Lin, J. Shui and H.-W. Liang, *Science*, 2021, **374**, 459–464.
12. J. Liang, N. Li, Z. Zhao, L. Ma, X. Wang, S. Li, X. Liu, T. Wang, Y. Du, G. Lu, J. Han, Y. Huang, D. Su and Q. Li, *Angew. Chem. Int. Ed.*, 2019, **58**, 15471–15477.
13. J. Li, S. Sharma, K. Wei, Z. Chen, D. Morris, H. Lin, C. Zeng, M. Chi, Z. Yin, M. Muzzio, M. Shen, P. Zhang, A. A. Peterson and S. Sun, *J. Am. Chem. Soc.*, 2020, **142**, 19209–19216.
14. T. Wang, J. Liang, Z. Zhao, S. Li, G. Lu, Z. Xia, C. Wang, J. Luo, J. Han, C. Ma, Y. Huang and Q. Li, *Adv. Energy Mater.*, 2019, **9**, 1803771.
15. Y. Yan, J. S. Du, K. D. Gilroy, D. Yang, Y. Xia and H. Zhang, *Adv. Mater.*, 2017, **29**, 1605997.
16. J. Liang, Y. Wan, H. Lv, X. Liu, F. Lv, S. Li, J. Xu, Z. Deng, J. Liu, S. Zhang, Y. Sun, M. Luo, G. Lu, J. Han, G. Wang, Y. Huang, S. Guo and Q. Li, *Nat. Mater.*, 2024, **23**, 1259–1267.
17. R.-Y. Shao, X.-C. Xu, Z.-H. Zhou, W.-J. Zeng, T.-W. Song, P. Yin, A. Li, C.-S. Ma, L. Tong, Y. Kong and H.-W. Liang, *Nat. Commun.*, 2023, **14**, 5896.
18. Z. Chen, J. Liu, B. Yang, M. Lin, C. Molochas, P. Tsiakaras and P. Shen, *J. Colloid Interface Sci.*, 2023, **652**, 388–404.
19. Y. Yu, W. Yang, X. Sun, W. Zhu, X. Z. Li, D. J. Sellmyer and S. Sun, *Nano Lett.*, 2014, **14**, 2778–2782.
20. A. Cebollada, D. Weller, J. Sticht, G. R. Harp, R. F. C. Farrow, R. F. Marks, R. Savoy and J. C. Scott, *Phys. Rev. B*, 1994, **50**, 3419‑3422.
21. T. Degen, M. Sadki, E. Bron, U. König and G. Nénert, *Powder Diffr.*, 2014, **29**, S13–S18.
22. T. Ozaki, *Phys. Rev. B*, 2003, **67**, 155108.
23. A. van de Walle, P. Tiwary, M. de Jong, D. L. Olmsted, M. Asta, A. Dick, D. Shin, Y. Wang, L. Q. Chen and Z. K. Liu, *Calphad*, 2013, **42**, 13–18.
24. S. Takamoto, C. Shinagawa, D. Motoki, K. Nakago, W. Li, I. Kurata, T. Watanabe, Y. Yayama, H. Iriguchi, Y. Asano, T. Onodera, T. Ishii, T. Kudo, H. Ono, R. Sawada, R. Ishitani, M. Ong, T. Yamaguchi, T. Kataoka, A. Hayashi, N. Charoenphakdee and T. Ibuka, *Nat. Commun.*, 2022, **13**, 2991.
25. C. Huang, H. Liu, Y. Tang, Q. Lu, S. Chu, X. Liu, B. Shan and R. Chen, *Appl. Catal. B: Environ.*, 2023, **320**, 121986.
26. A. Miura, H. Wang, B. M. Leonard, H. D. Abruña and F. J. DiSalvo, *Chem. Mater.*, 2009, **21**, 2661–2667.
27. S. Mourdikoudis and L. M. Liz-Marzán, *Chem. Mater.*, 2013, **25**, 1465–1476.
28. G. Feng, F. Ning, Y. Pan, T. Chen, J. song, Y. Wang, R. Zou, D. Su and D. Xia, *J. Am. Chem. Soc.*, 2023, **145**, 11140–11150.
29. Z. Cui, H. Chen, M. Zhao and F. J. DiSalvo, *Nano Lett.*, 2016, **16**, 2560–2566.
30. K. Takanashi, S. Mitani, M. Sano, H. Fujimori, H. Nakajima and A. Osawa, *Appl. Phys. Lett.*, 1995, **67**, 1016–1018.
31. S. Sun, C. B. Murray, D. Weller, L. Folks and A. Moser, *Science*, 2000, **287**, 1989–1992.
32. G. Kim, T. Hiratsuka, H. Naganuma, M. Oogane and Y. Ando, *J. Phys.: Conf. Ser.*, 2010, **200**, 052011.
33. R. A. Ristau, K. Barmak, L. H. Lewis, K. R. Coffey and J. K. J. J. o. A. P. Howard, *J. Appl. Phys.*, 1999, **86**, 4527–4533.
34. A. Kulkarni, S. Siahrostami, A. Patel and J. K. Nørskov, *Chem. Rev.*, 2018, **118**, 2302–2312.
35. Z. Wang, Y. Mai, Y. Yang, L. Shen and C. Yan, *ACS Appl. Mater. Interfaces*, 2021, **13**, 38138–38146.
36. Z. Wang, Y. Yang, X. Wang, Z. Lu, C. Guo, Y. Shi, H. Tan, L. Shen, S. Cao and C. Yan, *J. Mater. Chem. A*, 2022, **10**, 12141–12149.
37. Y. Zhou, Z. Zhou, R. Shen, R. Ma, Q. Liu, G. Cao and J. Wang, *Energy Storage Mater.*, 2018, **13**, 189‒198.
38. X. Xie, A. L. M. Sandhya, L. Piliai, M. Vorokhta, I. Motolínová and I. Khalakhan, *Appl. Catal. B*, 2023, **325**, 122328.
39. C. Lim, A. R. Fairhurst, B. J. Ransom, D. Haering and V. R. Stamenkovic, *ACS Catal.*, 2023, **13**, 14874–14893.
40. M. Gatalo, A. M. Bonastre, L. J. Moriau, H. Burdett, F. Ruiz-Zepeda, E. Hughes, A. Hodgkinson, M. Šala, L. Pavko, M. Bele, N. Hodnik, J. Sharman and M. Gaberšček, *ACS Appl. Energy Mater.*, 2022, **5**, 8862‒8877.
41. X. Tong, J. Zhang, G. Zhang, Q. Wei, R. Chenitz, J. P. Claverie and S. Sun, *Chem. Mater.*, 2017, **29**, 9579–9587.

Journal Name ARTICLE

View Article Online
DOI: 10.1039/D5TA08256K

View Article Online
DOI: 10.1039/D5TA08256K

The data supporting this article have been included as part of the Supplementary Information.